ARTICLES
PUBLISHED ONLINE: 26 MAY 2013 | DOI: 10.1038/NGEO1825

nature geoscience

Hydrogen generation from low-temperature water–rock reactions

L. E. Mayhew[1]*, E. T. Ellison[1], T. M. McCollom[2], T. P. Trainor[3] and A. S. Templeton[1]

Hydrogen is commonly produced during the high-temperature hydration of mafic and ultramafic rocks, owing to the oxidation of reduced iron present in the minerals. Hydrothermal hydrogen is known to sustain microbial communities in submarine vent and terrestrial hot-spring systems. However, the rates and mechanisms of hydrogen generation below temperatures of 150 °C are poorly constrained. As such, the existence and extent of hydrogen-fuelled ecosystems in subsurface terrestrial and oceanic aquifers has remained uncertain. Here, we report results from laboratory experiments in which we reacted ground ultramafic and mafic rocks and minerals—specifically peridotite, pyroxene, olivine and magnetite—with anoxic fluids at 55 and 100 °C, and monitored hydrogen gas production. We used synchrotron-based micro-X-ray fluorescence and X-ray absorption near-edge structure spectroscopy to identify changes in the speciation of iron in the materials. We report a strong correlation between molecular hydrogen generation and the presence of spinel phases—oxide minerals with the general formula $[M^{2+}M_2^{3+}]O_4$ and a cubic crystal structure—in the reactants. We also identify Fe(III)-(hydr)oxide reaction products localized on the surface of the spinel phases, indicative of iron oxidation. We propose that the transfer of electrons between Fe(II) and water adsorbed to the spinel surfaces promotes molecular hydrogen generation at low temperatures. We suggest that these localized sites of hydrogen generation in ultramafic aquifers in the oceanic and terrestrial crust could support hydrogen-based microbial life.

Serpentinization, the process of hydration of ultramafic rocks accompanied by H_2 production, fuels H_2-based microbial ecosystems such as at Lost City[1,2] and Rainbow hydrothermal vent systems[3,4]. The oxidation of Fe(II) in primary minerals to Fe(III) in secondary minerals reduces water to H_2 gas. This process is well studied at ≥200 °C (for example, refs 5–10). However, less is known about the potential for H_2-generating water–rock reactions to support rock-hosted microbial ecosystems when these reactions occur within the known temperature limit of life (~122 °C; ref. 11). In systems where H_2 generation could occur at low temperatures (for example, The Cedars, California[12]; Lost City[13]; Samail Ophiolite, Oman[14]) the production of H_2 in sufficient quantities and rates[15] to support subsurface H_2-using life (for example, SLiMEs (ref. 16)) is questioned[7]. Examination of naturally serpentinized rocks and geochemical models suggest that partitioning of Fe(III) into serpentine (relative to magnetite) and Fe(II) into secondary minerals such as brucite increases with decreasing reaction temperatures, resulting in less H_2 produced per mole of mineral reacted[7,8,17]. However, few laboratory investigations of H_2 production from water–rock reactions at <200 °C have been conducted and none has examined the secondary mineral products[18–20]. To address the outstanding questions concerning the amount, rate and mechanisms of H_2 generation at low temperatures, we conducted laboratory experiments at 55 and 100 °C with natural peridotite, olivine with high and low Fe contents (Fo_{12}, Fo_{90}), clinopyroxene with high and low Fe contents (hedenbergite, petedunnite), and magnetite. All of the reactants included minor mineral phases that in many cases played an important and previously overlooked role in the H_2-generating reactions (Table 1).

Low-T water–rock reaction experiments produce H_2

Experiments with San Carlos peridotite, San Carlos olivine, fayalite, magnetite and petedunnite, a Zn- and Mn-bearing pyroxene, produced H_2 above background levels during reaction at 55 and 100 °C (Fig. 1). We observed considerable variability in the amount of H_2 produced between replicate experiments of a single substrate. Only a fraction of the substrate reacted and equilibrium conditions were not reached. For some substrates, the variation in H_2 production was large enough that some replicates at 55 °C produced more H_2 than replicates at 100 °C. Thus, temperature was not the only variable affecting the amount of H_2 produced by a single substrate. We also observed variation between substrates, with a range of approximately 50–300 nmol H_2 produced per gram of mineral depending on the substrate. For substrates within the same mineral group (for example, olivines or clinopyroxenes), we expected H_2 production to vary with Fe(II) content (Supplementary Table S1). Indeed, fayalite (1.84 mol Fe per formula unit (pfu)) generated more H_2 than San Carlos olivine (0.2 mol Fe pfu). However, petedunnite (0.3 mol Fe pfu) produced much more H_2 than hedenbergite (0.8 mol Fe pfu), which had an average H_2 concentration not statistically greater than that observed in the media-only controls. This suggests that Fe content was not the only variable that influenced the amount of H_2 produced by different mineral phases within the same mineral group. The trend in H_2 production also could not be predicted from the bulk surface area of the substrates; for instance, hedenbergite had the highest surface area but produced the least H_2 (Table 1). The variation in H_2 production observed between replicate experiments of a single substrate and the lack of simple trends in H_2 production with temperature, Fe content or surface

[1]Department of Geological Sciences, UCB 399, University of Colorado—Boulder, Boulder, Colorado 80309, USA, [2]Laboratory for Atmospheric and Space Physics, UCB 392, University of Colorado—Boulder, Boulder, Colorado 80309, USA, [3]Department of Chemistry and Biochemistry, PO Box 756160, University of Alaska—Fairbanks, Fairbanks, Alaska 99775, USA. *e-mail: mayhewl@colorado.edu

Table 1 | The modal abundance (volume per cent) of each phase present in the starting geologic materials as obtained from QEMSCAN analyses.

Mineral phase	Fayalite	Magnetite	San Carlos olivine	Hedenbergite	Petedunnite	San Carlos peridotite
Olivine	86.9	40.0	90.8	0.2	0.6	85.3
Orthopyroxene	0.6	1.0	3.5	0	0	2.4
Clinopyroxene	6.2	1.8	0	80.4	1.1	3.8
Petedunnite	0	0	0	9.8	85.2	0
Amphibole	2.4	1.6	0	0.9	0.1	0
Fe(III)-bearing oxides*	0.4	43.6	0	0	0	0
Gahnite	0	0	0	0	1.2	0
Chromite	0	0	0.05	0	0	0.7
Other spinels	0	0	0.1	0	0	0.2
Siderite	1	3.2	0.7	5.6	0.7	1.9
Other carbonates	0	0	0	0.2	3.6	0.1
Chlorite	0.2	0.2	1.3	0	0	1.6
Talc	0	0	0.1	0	0	1.6
Serpentine	0	0	1.4	0	0	0.8
Secondary phases						
Fe(III)-(hydr)oxides	X	X	X	X	X	X
Fe(II)-silicate	X	?		X	X	
Fe(II)-brucite		?	X			X
Specific surface area (m^2 g^{-1})						
	0.2506 ± 0.0072	0.5738 ± 0.0063	0.2728 ± 0.0102	6.9959 ± 0.0702	0.2806 ± 0.0078	0.3442 ± 0.0052

The secondary phases detected in each experiment are indicated by an X. *category includes magnetite, haematite and goethite owing to difficulties distinguishing between them because of their similar Energy-dispersive X-ray spectroscopy spectra and backscattered electron signals.

area suggest that other parameters influence the processes and pathways of H_2 production.

Identification of rare, microscale reaction products

To identify the reactions controlling H_2 generation the solid-phase reaction products need to be identified, which poses a challenge due to the low abundance of secondary products and the heterogeneous nature of the substrates before incubation. Characterization of the starting materials and reacted samples using synchrotron-based X-ray fluorescence (μXRF) microprobe mapping at multiple energies within the Fe K-edge (Supplementary Figs S1 and S2, Figs 2 and 3) and Fe K-edge X-ray absorption near-edge structure (μXANES) spectroscopy (Supplementary Fig. S3) enabled direct comparisons between the unreacted and reacted materials. We were able to identify unique secondary products (Table 1) despite their limited abundance and predominant occurrence as surface coatings on primary phases.

Ferric iron products were detected in the experiments after H_2 generation, consistent with the reported formation of Fe(III)-oxides in olivine–water reactions conducted at 120 °C (ref. 21). Owing to the near-edge spectral characteristics (peak position, structure) for potential candidate (hydr)oxides (for example, ferrihydrite, haematite and goethite), we cannot uniquely identify the Fe(III)-bearing phase and henceforth use the term Fe(III)-(hydr)oxides to indicate Fe bound to O and/or OH in a variety of crystal structures. However, it is possible to quantitatively distinguish among the other classes of Fe-bearing phases detected in this work (for example, olivine, pyroxene, Fe(III)-(hydr)oxides, talc, brucite) on the basis of the spectral absorption edge and structure (Supplementary Fig. S4). These analyses reveal that the Fe(III)-bearing reaction products are non-silicate phases.

Fe(III)-(hydr)oxide products are a discrete phase in the fayalite and magnetite experiments, and synchrotron analyses also revealed the strong co-localization of Fe(III)-(hydr)oxides with primary spinel mineral phases (for example, magnetite, chromite and gahnite) in all experiments generating significant H_2. In the fayalite experiment, microscale secondary Fe(III)-(hydr)oxides were detected on the surfaces of magnetite particles that were present as impurities in the fayalite sample (Fig. 2). In the San Carlos peridotite, the oxidized Fe component was observed on chromite particles, which were identified optically and by trace-element μXRF microprobe mapping (Fig. 3a–c). In the petedunnite experiment, the distribution of Fe(III)-(hydr)oxides was correlated with Zn hotspots visible in trace-element maps (Fig. 3d–f) and the likely location of the Zn-bearing spinel particles that were identified as a minor phase by X-ray diffraction. Fe(III)-(hydr)oxides occurred in limited abundance in the San Carlos olivine experiment (Supplementary Fig. S2). The Fe(III)-(hydr)oxides observed in the hedenbergite experiment were not associated with spinel particles as there were no spinel phases present in the starting material; instead they were detected as discrete Fe(III)-(hydr)oxide particles (Supplementary Fig. S2). Although it seems that Fe(II) oxidation occurred in the hedenbergite experiment, spinels were evidently not the catalyst, and H_2O was not the oxidant because no H_2 production was observed; any redox processes occurring in this experiment remain uncertain. In summary, Fe(II) was oxidized to Fe(III) in all experiments but H_2 gas was detected only in experiments containing spinel phases.

The lack of experimental data on H_2 generation and secondary mineral production from low-temperature water–rock reactions necessitates comparisons to geochemical equilibrium models of peridotite- and olivine–water reactions. Models that extend below

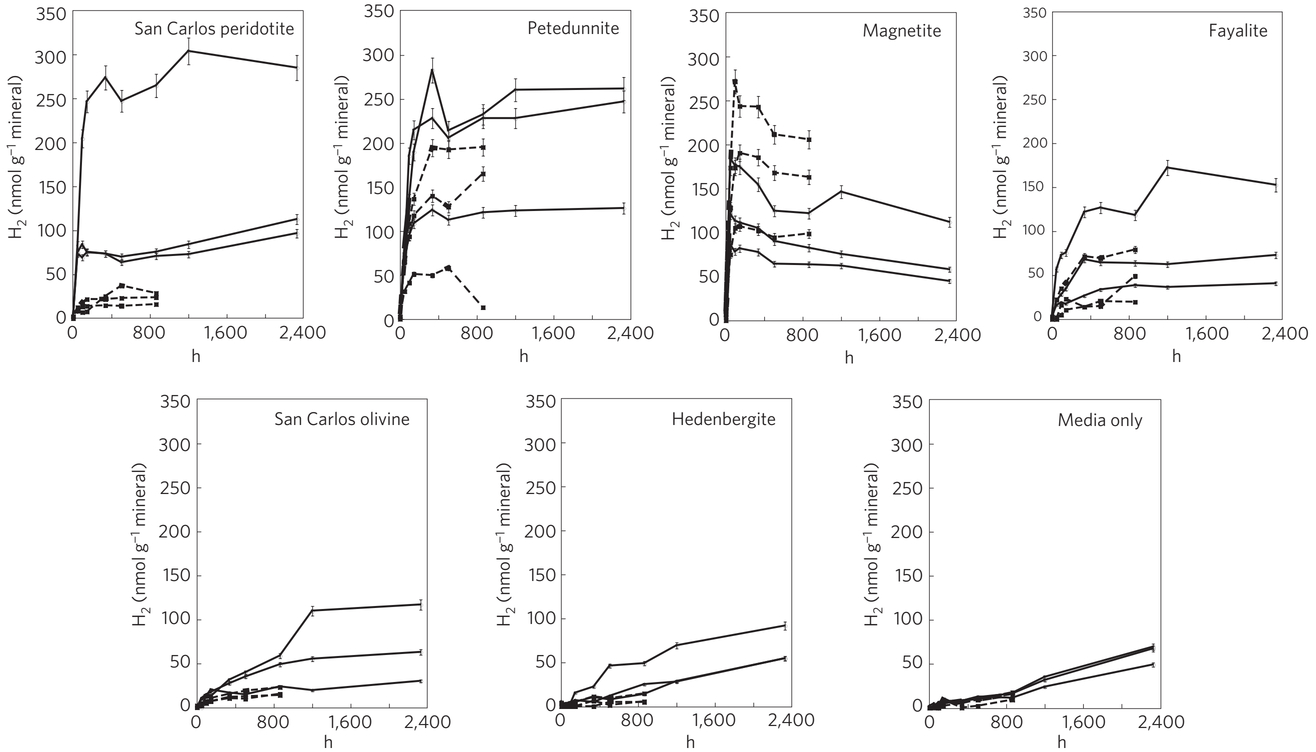

Figure 1 | Hydrogen production from water–rock reactions at 55 and 100 °C. The amount of H_2 gas (nanomoles) produced per gram of rock or mineral reacted is plotted versus reaction time. Each line represents a single experimental vial. Dashed lines represent data from 55 °C and solid lines represent data from 100 °C. Error bars represent the analytical uncertainty of the gas chromatography measurements (=5%).

200 °C correlate H_2 generation to the incorporation of Fe(III) into serpentine (for example, refs 7,8). The partitioning of Fe(III) into serpentine has also been documented in natural and experimental samples serpentinized at higher temperatures (for example, refs 6,17). Unlike equilibrium models, our experiments do not reach equilibrium conditions with respect to the aqueous geochemistry or H_2 activity and therefore non-equilibrium reaction products may be expected.

We do not detect serpentine in our peridotite and olivine experiments. Mineral stability diagrams (Supplementary Fig. S5) replicating the aqueous geochemistry at the time the solid phases were analysed predict the formation of a Fe-bearing talc in the fayalite, petedunnite and hedenbergite experiments due to high Si activity (Supplementary Table S2). We do detect Fe-bearing talc ($Mg_xFe_{3-x}Si_4O_{10}(OH)_2$) not present before reaction in these experiments. In natural systems, Fe-bearing talc is an alteration product when the amount of Si is high relative to Mg and Fe (for example, in the presence of basalt or pyroxene or when $(Mg+Fe)/Si < 1.5$). The talc in our experiments is Fe(II)-bearing (Supplementary Fig. S4), and preferentially coats the clinopyroxene particles, present as impurities in the fayalite sample (Fig. 2) and as the main components of the petedunnite and hedenbergite experiments (Fig. 3d,f and Supplementary Fig. S2).

In the San Carlos peridotite and San Carlos olivine experiments, Fe(II)-bearing brucite coatings ($Mg_xFe_{1-x}(OH)_2$) were observed on the olivine particles (Fig. 3a,c and Supplementary Fig. S2). The precipitation of brucite despite the high Si_{aq} of the bulk fluid (Supplementary Table S2 and Fig. S5) may be due to interfacial microenvironments with lower Si_{aq} activities. Together, the precipitation of Fe(II)-bearing brucite and talc suppresses H_2 generation by making Fe(II) solubilized from the primary minerals unavailable for oxidation. Furthermore, the incorporation of Fe(II) into secondary phases illustrates that only a fraction of the Fe(II) was oxidized to Fe(III).

Spinel-surface-promoted H_2 production

Hydrogen generation results indicate a strong correlation between the presence of spinels in the starting materials and the ability of a system to produce H_2. In the synchrotron-based Fe distribution and speciation results, we note that H_2 generation is correlated with samples where Fe(III)-(hydr)oxide products are co-localized with spinel surfaces. As we discuss below, these coupled observations clarify the inconsistent correlations between H_2 production and temperature, Fe content or surface area in these experiments. Furthermore, these observations may explain the variability in previously published work where solid-phase transformations were not investigated. We propose that electron transfer from spinel particles to adsorbed water molecules or protons is the predominant pathway for H_2 generation[22,23] in the low-temperature systems studied here (Fig. 4). The process and rates of electron transfer from $Fe(II)_{aq}$ to water are not well understood. As such, spinels may play an important role in promoting H_2 generation. Minerals with an inverse spinel structure are known to be highly conductive (for example, refs 24,25) and, in the case of magnetite, this is due to high electron mobility between Fe(II) and Fe(III) (ref. 26). Spinels are known to transfer electrons to oxidized metals present in soils and fluids and thus play a critical role in reducing metal contaminants (for example, refs 27–29). Spinels, including magnetite and chromite, have been proposed to catalyse organic synthesis reactions at high[30,31] and low[19] temperatures, but the mechanism has not been investigated. Intriguingly, much less is known or speculated about spinel-mediated transfer of electrons to water (or protons), although the sorption of water molecules to spinel surfaces has been documented (for example, refs 23,32–34).

During the proposed reaction, structural Fe(II) present in the spinels will be oxidized to Fe(III) resulting in the cessation of H_2 production without the addition of an external source of electrons. Sustained H_2generation could be realized using Fe(II) (aq) as an external source, through the dissolution of primary Fe-bearing

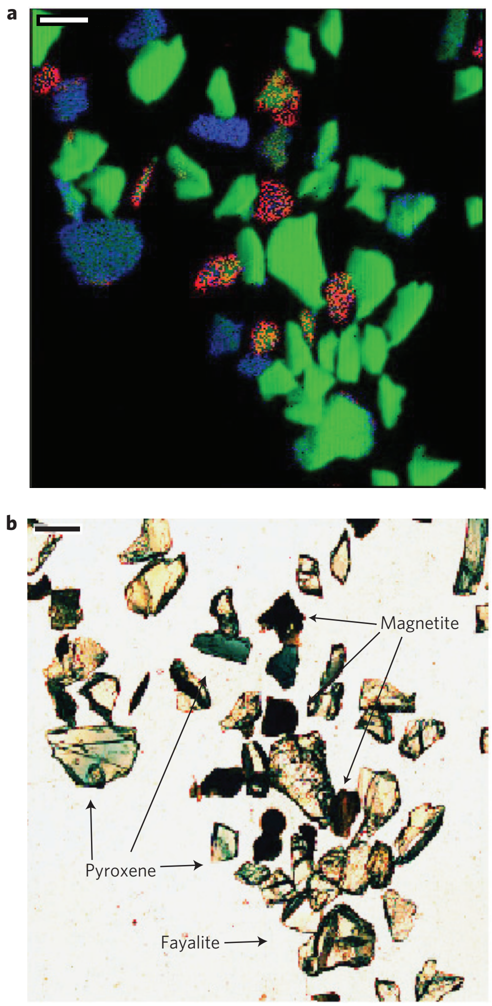

Figure 2 | Distribution of minerals in the fayalite experiment reacted at 100 °C. a, Mineral map generated from fitting representative XANES spectra to the Fe K-edge multiple energy maps. (red, Fe(III)-(hydr)oxides; green, fayalite; blue, Fe-bearing talc + fayalite). Fe(III)-(hydr)oxides correspond with magnetite particles and Fe-bearing talc corresponds with pyroxene particles as seen in **b**. **b**, Plane light photomicrographs of the mapped area. Scale bars, 90 μm.

silicates (Supplementary Table S2). Aqueous Fe(II) should strongly interact with the spinels and serve as an electron source, which is well documented for Fe oxides and spinels[35–37]. This results in the rapid oxidation of the sorbed Fe(II) due to the transfer of electrons from aqueous Fe(II) to the spinel substrate (for example, refs 35–39; Fig. 4b). Thus, aqueous Fe(II) may be an important source of electrons in these experiments.

Using the framework of spinel-surface-promoted H_2 production, we can explain the variation in the amount of H_2 produced from the different substrates tested in these experiments. We find that for all substrates containing trace spinels (0–1.2 vol%) there is a strong correlation between average spinel abundance (volume per cent per substrate) and average H_2 production ($R^2 = 0.97$, $P = 0.002$). Although the magnetite experiments (43.6 vol%) produced less H_2 than predicted by spinel volume per cent, thermodynamic calculations indicate that this system reached equilibrium with the magnetite–haematite buffer and was not surface-area limited. The spinel surface area in each experiment could not be independently measured and is likely to vary between each replicate experiment owing to uneven sub-sampling of the substrates. Differences in the amount of minor phases, and thus the spinel surface area, between replicate experiments may explain the high variability between replicates. Similarly, the flux of Fe_{aq} is an important control on H_2 production but this cannot be quantified because the concentration of Fe_{aq} in most experiments at most time points was below the detection limit of our analytical methods (Supplementary Table S2).

In most of the experiments, we observed H_2 generation to significantly decrease with reaction time. In closed-system experiments, it can be expected that the accumulation of reaction products can inhibit the forward reaction. However, flushing the headspace with N_2/CO_2 (chosen to mimic a system where CO_2 is the carbon source for chemolithoautotrophic microbial life) did not result in the re-initiation of H_2 production, suggesting that the reaction was not thermodynamically inhibited. In studies of the kinetics of mineral dissolution, initial rapid reaction rates are often attributed to the creation of highly reactive surface sites by mineral grinding (for example, ref. 40). A similar effect may occur in our experiments; however, we document H_2 production on the order of one to a few weeks depending on substrate. We suggest that the cessation of H_2 production may instead be due to two critical factors. First, H_2 generation may be limited by changes in the reduction potential and reactivity of the spinel catalysts. For example, the oxidation of surface Fe(II) atoms in magnetite has been observed to occur on the order of a few minutes to hours (for example, refs 26,27,41), followed by a decrease in reaction rates[41]. Second, the formation of secondary surface layers, such as Si-rich surface layers commonly formed by both incongruent dissolution and dissolution/reprecipitation processes (for example, refs 36,41–43), may inhibit the continued dissolution of olivine and pyroxene, thereby limiting the release of Fe(II) to solution and removing an important electron source for H_2 production. Thus, H_2 generation may be episodic depending on the rates of formation and destabilization of mineral surface layers during progressive water–rock interaction in an open system.

Furthering our understanding of low-T H_2 production

So far, the reaction(s) giving rise to H_2 production from water–rock reactions at low temperatures has not been identified. In contrast to the predicted formation of Fe(III)-serpentine (or Fe(III)-talc in the case of our high [Si_{aq}]) at low temperatures, we observe the partitioning of Fe released from olivine and pyroxene dissolution into Fe(III)-(hydr)oxides and Fe(II)-talc. Although we cannot quantify the total fraction of Fe in each phase, these observations have extended our understanding of changes in Fe speciation during low-temperature H_2 production. Previous experiments that produced measurable amounts of H_2 gas from ferrous silicates at 30–70 °C revealed inconsistencies in the variables that seem to affect H_2 production[18,19]. Both studies showed variation between replicate experiments; ref. 18 found a correlation between H_2 production and temperature whereas ref. 19 did not. The use of natural materials, which probably contained minor phases (for example, spinels), may explain the variation in the amount of H_2 generated. In fact, although we did not detect methane in our experiments at any time or temperature, ref. 19 attributes methane formation in its experiments to catalysis by spinel phases. On the basis of ref. 44 (namely, the reduction potential of Fe(II) is greater at solid–solution interfaces than in the aqueous phase), ref. 18 suggested that surface Fe(II), whether an intrinsic component of the minerals or adsorbed to a solid Fe-bearing surface, may have participated in the H_2 producing reactions. Our hypothesis of spinel-surface-promoted electron transfer also supports the important role of surface Fe(II) in H_2-producing reactions.

Potential role of spinels in natural geologic systems

Our ability to detect, identify and assess the distribution of secondary phases has further elucidated the reactions responsible for low-temperature H_2 production. The model of spinel-surface-

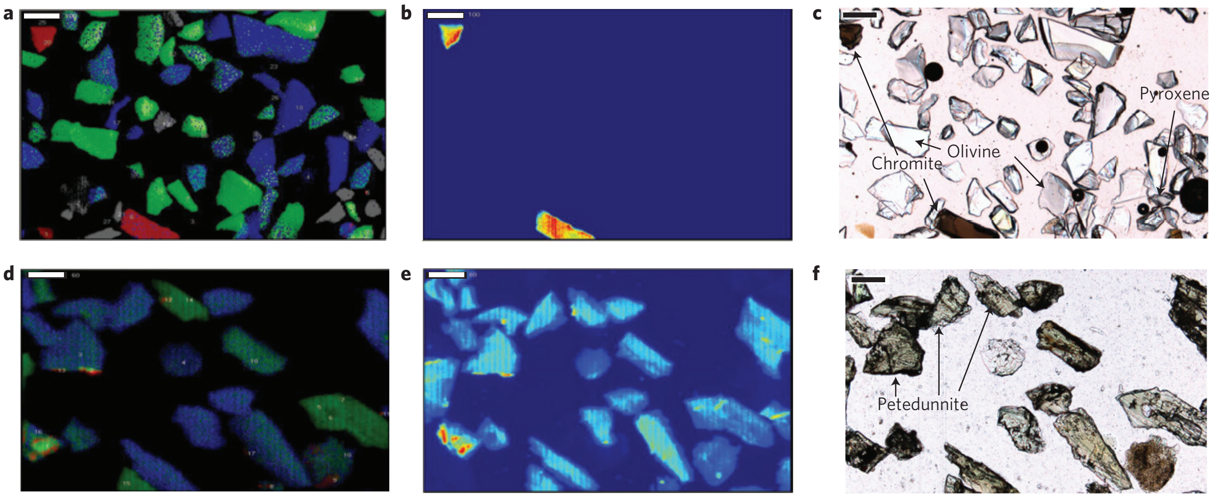

Figure 3 | Geochemical maps of San Carlos peridotite and petedunnite reacted at 100 °C. a, Mineral distribution in reacted San Carlos peridotite. (red, Fe(III)-(hydr)oxides; green, olivine; blue, olivine + brucite; grey, pyroxene). **b**,**c**, Fe(III)-(hydr)oxides coat chromite particles identified in the map of chromium distribution (**b**) and the plane light photomicrograph (**c**). Scale bars, 100 μm. **d**, Mineral distribution in reacted petedunnite (red, Fe(III)-(hydr)oxides; green, pyroxene; blue, Fe-talc). **e**, Fe(III)-(hydr)oxide coatings correspond with zinc hotspots (that is, $ZnAl_2O_4$ (gahnite)) identified in the map of zinc distribution. **f**, Fe(II)-talc coats many pyroxenes seen in the plane light photomicrograph. Scale bars, 60 μm.

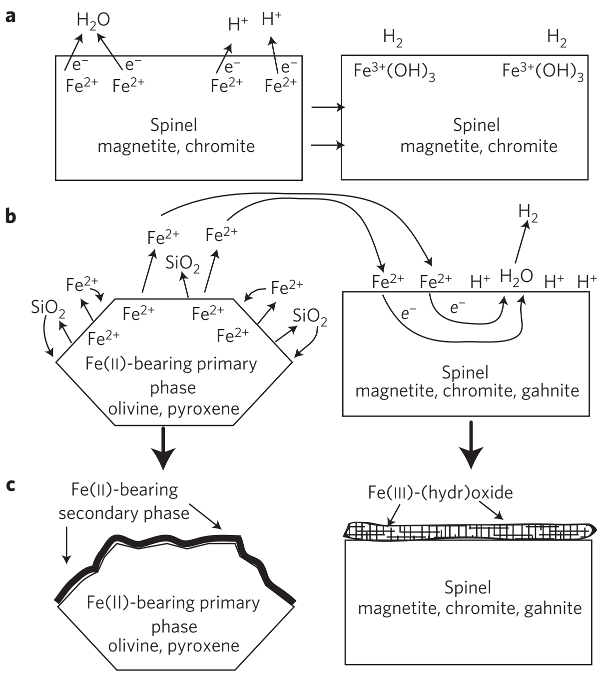

Figure 4 | Schematic representation of spinel-surface-promoted H_2 generation. Hydrogen is produced when: **a**, water molecules and protons adsorb to spinel surfaces, and electrons are transferred to adsorbed water/protons from structural Fe(II); and **b**, dissolution of Fe(II)-bearing silicates releases Fe(II) and SiO_2(aq) to solution. Fe(II) adsorbs to spinel surfaces and participates in interfacial electron transfer, resulting in sustained reduction of water and/or protons. **c**, Hydrogen generation may cease when localized precipitation of secondary surface layers diminishes the release of Fe(II) from the primary silicate, and/or oxidation of spinel surface Fe(II) atoms and adsorbed Fe(II) produces an oxidized surface layer passivating the spinel.

promoted electron transfer not only provides a framework for understanding the mechanism of H_2 production in our mineralogically complex experimental system but also provides a testable hypothesis that can be further investigated mechanistically and in natural samples. Furthermore, there is great potential for inherent spinel reactivity and interfacial electron transfer processes between adsorbed Fe(II) and spinels to drive H_2 generation in low-temperature oceanic and terrestrial aquifers. Partially reacted (ultra)mafic rocks, which often possess high spinel contents, would be particularly inclined to produce significant amounts of H_2 during continued low-temperature hydration and alteration, depending on the extent of surface passivation.

In these geologic settings, spinel-promoted electron transfer would produce a critical energy source for subsurface lithoautotrophic communities (for example, SLiMEs (ref. 16)), including methanogens, and as such may affect the fate of CO_2 in peridotites and basalts. The presence of H_2-driven microbial communities could greatly affect the fate of deep subsurface carbon and the progression of coupled hydration and carbonation reactions. Proposals to drill into low-temperature reaction zones of (ultra)mafic rocks (for example Lost City, Mid-Atlantic Ridge; Oman; California Coast Range) may soon provide opportunities to directly investigate the alteration processes and associated subsurface biosphere. The possibility exists that some organisms may be capable of enzymatically coupling the oxidation of Fe(II) to the reduction of H_2O, thereby rendering the geochemical production of H_2 an extraneous electron-transfer step; however, this biological capability has not yet been demonstrated. One intriguing hypothesis we can propose is the potential for microorganisms to preferentially position themselves adjacent to spinel particles to maximize their ability to consume H_2 as it is produced and perhaps even prevent spinel surface passivation. Material retrieved from actively reacting low-temperature geologic environments could be used for targeted searches (for example, using Raman microscopy or molecular investigations) for microbial organisms or biosignatures. Recently, high concentrations of organic matter were found in serpentinized rocks using such techniques[45]. Furthermore, discoveries of serpentinized rocks on Mars[46] suggest that spinel-surface-promoted H_2 production could have implications for potential microbial habitats on Mars and other terrestrial planetary bodies.

Methods

Peridotite and olivine (San Carlos), and fayalite and magnetite (Forsythe Iron Mine) were purchased from Ward's Scientific. Two clinopyroxenes, a hedenbergite (South Mountain, Oywhee) and a petedunnite (Nain, Labrador) were purchased from Excalibur Minerals. Materials were ground in a porcelain mortar, wet sieved with deionized water (53–212 μm), dried at room temperature, and imaged by scanning electron microscopy to verify removal of small grains. No metal tools were used. Mineral separates were purified using a hand magnet and a Frantz Magnetic Separator. Component identification and semi-quantitative mineral abundances were acquired by QEMSCAN scanning electron microscopy[47]. Quantitative weight per cent oxides of the major components were acquired by electron microprobe (JEOL JXA 8600). Surface area measurements were made using Micromeritics Gemini V (N_2 gas) and the Brunauer–Emmett–Teller method.

Experiments had a water/rock ratio of 7:1 (5 g rock, 35 ml sulphate-free artificial seawater media[48], except for fayalite, 1.5 g rock, 10 ml media). Media and glass serum vials were purged with 80% N_2, 20% CO_2 and the vials were capped with an airtight butyl rubber stopper boiled 3× in 0.1 mol NaOH l^{-1} (ref. 31). Experiments (including media-only) were conducted in triplicate at 55 and 100 °C. Vials were heated to 550 °C for 3 h to remove combustible carbon species. Geologic substrates were sterilized by oven heating at 100 °C for >24 h. Vials, rubber stoppers and media were autoclaved before experiment assembly.

An SRI 310C gas chromatograph with an Alltech Molecular Sieve (5A 80/100) 6′ × 0.085″ ID column and thermal conductivity detector using N_2 as the carrier gas was used to measure H_2. Methane was measured using a flame ionization detector and CO_2 was measured using a thermal conductivity detector on an SRI 8610C gas chromatograph with a PORAPAK Q 6′ × 0.085" I.D. column using He as the carrier gas. Removed headspace gas was replaced with sterile N_2 gas.

An inductively coupled optical emission spectrometer was used to measure aqueous concentrations of Fe, Si, Mg and Ca. Medium was aseptically removed from the experiments, filtered through a 0.2 μm sterile Millipore Millex filter, acidified with trace-metal-grade nitric acid, and diluted 10×. Medium removed was replaced with an equal volume of anaerobic medium.

Samples were prepared for optical imaging and synchrotron analyses in an anaerobic chamber to avoid exposure to oxygen. Mineral particles were removed using a 23 gauge needle, washed in anaerobic MilliQ water, applied to a pure quartz microscope slide (ESI), and dried at room temperature. Epoxy (Buehler) was applied to the dried sample that was then removed from the anaerobic chamber and hardened at 55 °C. To reduce potential oxidation of the sample, grains were exposed at the surface of the epoxy during dry grinding on silica carbide sandpaper, polished using 0.25 μm diamond in ethanol and cleaned with acetone.

Synchrotron-based hard-X-ray microprobe measurements were conducted at BL 2–3 at the Stanford Synchrotron Radiation Lightsource (SSRL). Fe K-edge mapping was conducted at 5 (7123, 7127, 7128, 7130, 7133 eV), 6 (+7129 eV), 7 (+7129, 7131) or 8 (+7126, 7129, 7131 eV) discrete energies, chosen to maximize the differences in normalized intensity between representative μXANES. The focused beam size was approximately 2 × 2 μm (pixel step-size = 2 or 4 μm). Maps were generated in a continuous scanning mode using a vortex detector; all windowed counts for each element extracted from the full X-ray fluorescence spectra were normalized to the intensity of the incident X-ray beam (I_0). Multiple energy XRF maps were dead time corrected and run through a principal components analysis using the MicroAnalysis Toolkit[49] producing maps of the spatial distribution of unique components, used to guide the selection of μXANES locations. Ten to 30 Fe K-edge spectra were collected from each map area. Principal components analysis of the normalized, dead-time-corrected, background-subtracted spectra was conducted using SIXPACK (ref. 50) to identify the spectra representative of each unique component within the sample (Supplementary Fig. S3). Maps were fitted with representative spectra to produce maps of the spatial distribution of each component.

To determine Fe speciation, representative spectra were fitted from 7,110 to 7,150 eV using linear combinations of Fe model compounds calibrated using the first inflection of a Fe^0 foil at 7,112 eV (Supplementary Fig. S4). The model compound library included iron-bearing minerals representing a diversity of mineral groups[48]. Fits were done using the Cycle Fit function in SIXPACK (ref. 50). Spectra were fitted individually as 1-component fits and then the fit cycle was repeated for 2-component fits using the best 1-component model compound paired with the remaining model compounds. This process is repeated until adding another component no longer decreases the R^2 value by 10% or greater.

Conventional powder X-ray diffraction (XRD; PANalytical XPert PRO MRD, Almelo) was used to obtain diffraction patterns from the un-reacted starting materials.

Received 19 October 2012; accepted 12 April 2013; published online 26 May 2013

References

1. Schrenk, M. O., Kelley, D. S., Bolton, S. A. & Baross, J. A. Low archaeal diversity linked to subseafloor geochemical processes at the Lost City Hydrothermal Field, Mid-Atlantic Ridge. *Environ. Microbiol.* **6,** 1086–1095 (2004).
2. Kelley, D. S. *et al.* A serpentinite-hosted ecosystem: The lost city hydrothermal field. *Science* **307,** 1428–1434 (2005).
3. Charlou, J. L., Donval, J. P., Fouquet, Y., Jean-Baptiste, P. & Holm, N. Geochemistry of high H-2 and CH_4 vent fluids issuing from ultramafic rocks at the Rainbow hydrothermal field (36 degrees 14'N, MAR). *Chem. Geol.* **191,** 345–359 (2002).
4. Flores, G. E. *et al.* Microbial community structure of hydrothermal deposits from geochemically different vent fields along the Mid-Atlantic Ridge. *Environ. Microbiol.* **13,** 2158–2171 (2011).
5. Moody, J. B. Serpentinization: A review. *Lithos* **9,** 125–138 (1976).
6. Seyfried, W. E., Foustoukos, D. I. & Fu, Q. Redox evolution and mass transfer during serpentinization: An experimental and theoretical study at 200 °C, 500 bar with implications for ultramafic-hosted hydrothermal systems at Mid-Ocean Ridges. *Geochim. Cosmochim. Acta* **71,** 3872–3886 (2007).
7. McCollom, T. M. & Bach, W. Thermodynamic constraints on hydrogen generation during serpentinization of ultramafic rocks. *Geochim. Cosmochim. Acta* **73,** 856–875 (2009).
8. Klein, F. *et al.* Iron partitioning and hydrogen generation during serpentinization of abyssal peridotites from 15 N on the Mid-Atlantic Ridge. *Geochim. Cosmochim. Acta* **73,** 6868–6893 (2009).
9. Jones, L. C., Rosenbauer, R., Goldsmith, J. I. & Oze, C. Carbonate control of H_2 and CH_4 production in serpentinization systems at elevated P-Ts. *Geophys. Res. Lett.* **37,** L14306 (2010).
10. Malvoisin, B., Brunet, F., Carlut, J., Roumejon, S. & Cannat, M. Serpentinization of oceanic peridotites: 2. Kinetics and processes of San Carlos olivine hydrothermal alteration. *J. Geophys. Res.* **117,** B04102 (2012).
11. Takai, K. *et al.* Cell proliferation at 122 °C and isotopically heavy CH_4 production by a hyperthermophilic methanogen under high-pressure cultivation. *Proc. Natl Acad. Sci. USA* **105,** 10949–10954 (2008).
12. Barnes, I. & O'Neil, J. R. The relationship between fluids in some fresh alpine-type ultramafics and possible modern serpentinization, western United States. *Geol, Soc. Amer. Bull.* **80,** 1947–1960 (1969).
13. Proskurowski, G., Lilley, M. D., Kelley, D. S. & Olson, E. J. Low temperature volatile production at the Lost City Hydrothermal Field, evidence from a hydrogen stable isotope geothermometer. *Chem. Geol.* **229,** 331–343 (2006).
14. Barnes, I., O'Neil, J. R. & Trescases, J-J. Present day serpentinization in New Caledonia, Oman and Yugoslavia. *Geochim. Cosmochim. Acta* **42,** 144–145 (1978).
15. Hoehler, T. M. Biological energy requirements as quantitative boundary conditions for life in the subsurface. *Geobiology* **2,** 205–215 (2004).
16. Nealson, K. H., Inagaki, F. & Takai, K. Hydrogen-driven subsurface lithoautotrophic microbial ecosystems (SLiMEs): do they exist and why should we care? *Trends Microbiol.* **13,** 405–410 (2005).
17. Evans, B. W., Kuehner, S. M. & Chopelas, A. Magnetite-free, yellow lizardite serpentinization of olivine websterite, Canyon Mountain complex, NE Oregon. *Am. Miner.* **94,** 1731–1734 (2009).
18. Stevens, T. O. & McKinley, J. P. Abiotic controls on H-2 production from basalt-water reactions and implications for aquifer biogeochemistry. *Environ. Sci. Technol.* **34,** 826–831 (2000).
19. Neubeck, A., Duc, N. T., Bastviken, D., Crill, P. & Holm, N. G. Formation of H_2 and CH_4 by weathering of olivine at temperatures between 30 and 70 °C. *Geochem. Trans.* **12,** 6 (2011).
20. Parkes, R. J. *et al.* Prokaryotes stimulate mineral H_2 formation for the deep biosphere and subsequent thermogenic activity. *Geology* **39,** 219–222 (2011).
21. Olsson, J. *et al.* Olivine reactivity with CO_2 and H_2O on a microscale: Implications for carbon sequestration. *Geochim. Cosmochim. Acta* **77,** 86–97 (2012).
22. Mancey, D., Shoesmith, D., Lipkowski, J., McBride, A. & Noel, J. An electrochemical investigation of the dissolution of magnetite in acidic electrolytes. *J. Electrochem. Soc.* **140,** 637–642 (1993).
23. Parkinson, G. S., Novotny, Z., Jacobson, P., Schmid, M. & Diebold, U. Room temperature water splitting at the surface of magnetite RID A-3681-2010. *J. Am. Chem. Soc.* **133,** 12650–12655 (2011).
24. Hamilton, W. Neutron diffraction investigation of the 119K Transition in Magnetite. *Phys. Rev.* **110,** 1050–1057 (1958).
25. Balko, B. & Hoy, G. Selective excitation double Mossbauer studies (SEDM) of electron hopping. *Physica B C* **86,** 953–954 (1977).
26. Skomurski, F. N., Kerisit, S. & Rosso, K. M. Structure, charge distribution, and electron hopping dynamics in magnetite (Fe3O4) (100) surfaces from first principles. *Geochim. Cosmochim. Acta* **74,** 4234–4248 (2010).
27. Peterson, M., Brown, G., Parks, G. & Stein, C. Differential redox and sorption of Cr(III/VI) on natural silicate and oxide minerals: EXAFS and XANES results. *Geochim. Cosmochim. Acta* **61,** 3399–3412 (1997).
28. White, A. & Peterson, M. Reduction of aqueous transition metal species on the surfaces of Fe(II)-containing oxides. *Geochim. Cosmochim. Acta* **60,** 3799–3814 (1996).
29. Shipley, H. J., Yean, S., Kan, A. T. & Tomson, M. B. Adsorption of arsenic to magnetite nanoparticles: Effect of particle concentration, pH, ionic strength, and temperature. *Environ. Toxicol. Chem.* **28,** 509–515 (2009).
30. Foustoukos, D. & Seyfried, W. Hydrocarbons in hydrothermal vent fluids: The role of chromium-bearing catalysts. *Science* **304,** 1002–1005 (2004).

31. Fu, Q., Lollar, B. S., Horita, J., Lacrampe-Couloume, G. & Seyfried, W. E. Abiotic formation of hydrocarbons under hydrothermal conditions: Constraints from chemical and isotope data. *Geochim. Cosmochim. Acta* **71,** 1982–1998 (2007).
32. Joseph, Y., Kuhrs, C., Ranke, W. & Weiss, W. Adsorption of water on Fe3O4(111) studied by photoelectron and thermal desorption spectroscopy. *Surf. Sci.* **433,** 114–118 (1999).
33. Kendelewicz, T. *et al*. Reaction of water with the (100) and (111) surfaces of Fe_3O_4. *Surf. Sci.* **453,** 32–46 (2000).
34. Petitto, S. C., Tanwar, K. S., Ghose, S. K., Eng, P. J. & Trainor, T. P. Surface structure of magnetite (111) under hydrated conditions by crystal truncation rod diffraction. *Surf. Sci.* **604,** 1082–1093 (2010).
35. Williams, A. & Scherer, M. Spectroscopic evidence for Fe(II)–Fe(III) electron transfer at the iron oxide-water interface. *Environ. Sci. Technol.* **38,** 4782–4790 (2004).
36. Silvester, E. *et al*. Redox potential measurements and Mossbauer spectrometry of Fe-II adsorbed onto Fe-III (oxyhydr)oxides RID A-1353-2010. *Geochim. Cosmochim. Acta* **69,** 4801–4815 (2005).
37. Tanwar, K. S., Petitto, S. C., Ghose, S. K., Eng, P. J. & Trainor, T. P. Structural study of Fe(II) adsorption on hematite(1(1)over-bar02). *Geochim. Cosmochim. Acta* **72,** 3311–3325 (2008).
38. Rosso, K. M., Yanina, S. V., Gorski, C. A., Larese-Casanova, P. & Scherer, M. M. Connecting observations of hematite (alpha-Fe(2)O(3)) growth catalyzed by Fe(II). *Environ. Sci. Technol.* **44,** 61–67 (2010).
39. Catalano, J. G., Fenter, P., Park, C., Zhang, Z. & Rosso, K. M. Structure and oxidation state of hematite surfaces reacted with aqueous Fe(II) at acidic and neutral pH RID A-8544-2008. *Geochim. Cosmochim. Acta* **74,** 1498–1512 (2010).
40. Mckibben, M. & Barnes, H. Oxidation of pyrite in low-temperature acidic solutions—Rate laws and surface textures. *Geochim. Cosmochim. Acta* **50,** 1509–1520 (1986).
41. White, A., Peterson, M. & Hochella, M. Electrochemistry and dissolution kinetics of magnetite and ilmenite. *Geochim. Cosmochim. Acta* **58,** 1859–1875 (1994).
42. Bearat, H. *et al*. Carbon sequestration via aqueous olivine mineral carbonation: Role of passivating layer formation. *Environ. Sci. Technol.* **40,** 4802–4808 (2006).
43. Schott, J., Pokrovsky, O. S. & Oelkers, E. H. in *Thermodynamics and Kinetics of Water–Rock Interaction* Vol. 70 (eds Oelkers, E. & Schott, J.) 207–258 (Mineralogical Soc. Amer., 2009).
44. White, A. & Yee, A. Aqueous oxidation–reduction kinetics associated with coupled electron cation transfer from iron-containing silicates at 25 °C. *Geochim. Cosmochim. Acta* **49,** 1263–1275 (1985).
45. Menez, B., Pasini, V. & Brunelli, D. Life in the hydrated suboceanic mantle. *Nature Geosci.* **5,** 133–137 (2012).
46. Ehlmann, B. L., Mustard, J. F. & Murchie, S. L. Geologic setting of serpentine deposits on Mars. *Geophys. Res. Lett.* **37,** L06201 (2010).
47. Hoal, K. O. *et al*. Research in quantitative mineralogy: Examples from diverse applications. *Miner. Eng.* **22,** 402–408 (2009).
48. Mayhew, L. E., Webb, S. M. & Templeton, A. S. Microscale imaging and identification of Fe speciation and distribution during fluid–mineral reactions under highly reducing conditions. *Environ. Sci. Technol.* **45,** 4468–4474 (2011).
49. Webb, S. M. The MicroAnalysis Toolkit: X-ray fluorescence image processing software. *AIP Conf. Proc.* **1365,** 196–199 (2011).
50. Webb, S. M. SIXPack: A graphical user interface for XAS analysis using IFEFFIT. *Phys. Scr.* **2005,** 1011–1014 (2005).

Acknowledgements
G. Lau and E. Swanner participated in collection of reference spectra. We thank the Smithsonian National Museum of Natural History for minerals used as Fe model compounds. We acknowledge F. Luiszer, J. Drexler and P. Boni, at the University of Colorado-Boulder, for IC-OES, ICP-MS and electron microprobe analyses, and sample preparation work, respectively. We thank F. Majs (U. Alaska) for conducting XRD analyses. This work was directly supported by the David and Lucille Packard Foundation (A.S.T.) and a DOE Early Career grant (A.S.T.) (DE-SC0006886). Synchrotron analyses were conducted on beamlines 2-3, 11-2, and 4-1 at the Stanford Synchrotron Radiation Lightsource (SSRL), a national user facility operated by Stanford University on behalf of the Department of Energy, Office of Basic Energy Sciences, through the Structural Molecular Biology Program, supported by DOE Office of Biological and Environmental Research and the National Institutes of Health.

Author contributions
L.E.M. and A.S.T. conceived of and designed the experiments. L.E.M. and E.T.E. assembled the experiments, conducted gas chromatography analyses, and sampled for aqueous, synchrotron and XRD analyses. L.E.M. and A.S.T. conducted synchrotron-based X-ray spectroscopy and microprobe mapping data collection. L.E.M. processed and analysed all data. L.E.M completed the data interpretation and wrote the manuscript with input and critical discussion from A.S.T., E.T.E., T.P.T. and T.M.M.

Additional information
Supplementary information is available in the online version of the paper. Reprints and permissions information is available online at www.nature.com/reprints. Correspondence and requests for materials should be addressed to L.E.M.

Competing financial interests
The authors declare no competing financial interests.